

# High-acoustic-index-contrast phononic circuits: numerical modeling

Wance Wang,<sup>1,2, a)</sup> Mohan Shen,<sup>1,2</sup> Chang-Ling Zou,<sup>1,2</sup> Wei Fu,<sup>1</sup> Zhen Shen,<sup>1,2</sup> and Hong X. Tang<sup>1, b)</sup>

<sup>1)</sup>*Department of Electrical Engineering, Yale University, New Haven, Connecticut 06511, USA*

<sup>2)</sup>*Department of Optics, University of Science and Technology of China, CAS, Hefei, Anhui 230026, China*

(ΩDated: 3 November 2020)

We numerically model key building blocks of a phononic integrated circuit that enable phonon routing in high-acoustic-index waveguides. Our particular focus is on Gallium Nitride-on-sapphire phononic platform which has recently demonstrated high acoustic confinement in its top layer without the use of suspended structures. We start with systematic simulation of various transverse phonon modes supported in strip waveguides and ring resonators with sub-wavelength cross-section. Mode confinement and quality factors of phonon modes are numerically investigated with respect to geometric parameters. Quality factor up to  $10^8$  is predicted in optimized ring resonators. We next study the design of the phononic directional couplers, and present key design parameters for achieving strong evanescent couplings between modes propagating in parallel waveguides. Last, interdigitated transducer electrodes are included in the simulation for direct excitation of a ring resonator and critical coupling between microwave input and phononic dissipation. Our work provides comprehensive numerical characterization of phonon modes and functional phononic components in high-acoustic-index phononic circuits, which supplements previous theories and contributes to the emerging field of phononic integrated circuits.

## I. INTRODUCTION

Surface acoustic wave (SAW) devices are widely used in electronic circuits, finding applications such as filters and oscillators in communication devices<sup>1</sup> and a range of sensing applications<sup>2-4</sup>. Recently, SAWs are also exploited for coherent control of various quantum systems, including the electron quantum dots<sup>5-7</sup>, electron spins in diamond<sup>8</sup>, superconducting qubits<sup>9-11</sup>, and integrated photonic devices<sup>12-15</sup>. Thus, SAW provides a promising platform for hybrid quantum systems<sup>16-19</sup>, where the traveling SAW phonon can serve as a quantum bus to facilitate quantum state transfer.

The coupling strength between SAW and matter/photons is enhanced with reduced mode volume of the SAW. The enhanced interactions such as the strong coupling regime of cavity quantum acoustodynamics<sup>20,21</sup> not only increases coherent coupling rates between quantum bits, but also improve the sensitivity of SAW-based measurements<sup>22</sup>. Also, the full potential of phononic systems can be only unraveled when maneuverability of phonon becomes comparable to its electrical and optical counterparts. Therefore, a strong confinement of the SAW to the diffraction limit and the long lifetime phononic resonators are in high demand. To that end, phonon waveguides<sup>23-25</sup> and ring resonators<sup>26,27</sup> based on SAW were proposed and experimentally studied in the 1970s. However, in the following several decades, the experiments and detailed theoretical studies of the confinement of itinerant phonons in microstructures were less active, especially for the phonon resonators of ra-

diating waves in nature. Only in recent years, due to the advances of nano-fabrication technologies, ultra-low loss phononic waveguides and resonators are achieved with bulk acoustic wave<sup>28,29</sup> and with SAW<sup>30-41</sup>, pushing the study of phononic devices, including SAW-related waveguides and resonators back to the frontier of researches as a strong contender for advanced phononic circuits.

Interdigital transducers (IDTs) convert the electrical RF signal into SAW or *vice versa* by employing the piezoelectric materials. In most applications, IDTs are fabricated on a uniform film, and the lateral size of IDT is much larger than the wavelength of SAW to excite and collect the quasi-collimated SAW. As a primary source or receiver of SAWs, the scaling of IDTs and their integration with other SAW devices is also in critical demand in the development of phononic circuits.

A variety of piezoelectric material platforms have been explored for SAW devices, including ST-X quartz<sup>20,22</sup>, zinc oxide<sup>42-44</sup>, lithium niobate<sup>10,45,46</sup>, lithium tantalate<sup>47</sup>, aluminum nitride<sup>48-51</sup>, gallium arsenide<sup>9,21,52,53</sup>, and gallium nitride<sup>41,54-56</sup>. Together with substrate material such as sapphire, diamond, and silicon, various combinations of high-acoustic-index-contrast SAW devices can provide better confinement and thus low loss, as well as the dispersion can be engineered. Table I summarizes common piezoelectric materials and substrates. Among these piezo-materials,  $\text{LiNbO}_3$  and  $\text{LiTaO}_3$  possess much larger electromechanical coupling coefficients ( $K^2$ ) than other materials, but they have poor temperature stabilities, whereas quartz is in a reverse case with weak coupling but good temperature stability at room temperature<sup>57</sup>.  $\text{ZnO}$  has wide bandgap<sup>58</sup> and good film stoichiometry<sup>59</sup> in addition to relatively large  $K^2$ <sup>60</sup>.  $\text{ZnO}$ /diamond is also a quantum interface between SAW and nitrogen-

<sup>a)</sup>Now at Department of Physics, University of Maryland, College Park.

<sup>b)</sup>Electronic mail: [hong.tang@yale.edu](mailto:hong.tang@yale.edu)

Material	$V_l$ ( $\text{m} \cdot \text{s}^{-1}$ )	$V_t$ ( $\text{m} \cdot \text{s}^{-1}$ )	Piezoelectricity
Quartz <sup>63</sup>	5700	3158	Weak
ZnO <sup>64</sup>	5790	2700	Strong
LiNbO <sub>3</sub> <sup>65</sup>	7316	4795	Strong
AlN <sup>66</sup>	10,169	6369	Good
GaN <sup>66</sup>	7350	4578	Good
Diamond <sup>67</sup>	18,000	12,000	No
Sapphire <sup>68</sup>	10,658	5796	No
SiO <sub>2</sub> <sup>69</sup>	8433	5843	No

TABLE I. SAW waveguide and substrate materials.  $V_l$ ,  $V_t$  are longitudinal and transverse wave speed, respectively.

vacancy center in diamond<sup>42</sup>. AlN has high refractive index and high phase velocity<sup>56,61</sup> which is in favor of high-frequency devices, but in turn, the contrast of acoustic index will be low. It also finds applications in high-temperature environments<sup>49</sup>. Semiconductor material GaN and GaAs are compatible with standard wafer-scale fabrication, GaAs is also naturally suited for InGaAs quantum dots<sup>53</sup> which benefit from the telecom range. The availability of GaN high-performance amplifiers enables monolithic integration with devices. For the layered system to our knowledge, ZnO/diamond, ZnO/sapphire, ZnO/SiO<sub>2</sub><sup>42,43,62</sup>, AlN/sapphire, AlN/SiO<sub>2</sub><sup>49,50</sup>, and GaN/sapphire<sup>56</sup> have been explored. Diamond the highest known SAW phase velocity but its fabrication requires chemical vapour deposition<sup>62</sup>, and it suffers from larger propagation loss. The contrast of SiO<sub>2</sub>-based platform isn't high. Concluding all factors, GaN/sapphire platform stands out as a high-performance and ready-access choice.

In this paper, we numerically investigate the properties of integrated phononic waveguides and resonators based on GaN-on-sapphire platform. Different from  $\Delta V/V$  confinement effect induced by the metal electrodes<sup>30–33,70</sup>, we consider the pure geometric confinement of phonon on the surface of the chip, thus the metal-induced loss is eliminated. We prove that the phononic ring resonator can have exceptionally high quality factors ( $Q$ ) with the radius of tens of microns, in which the whispering gallery modes (WGMs) can be excited either by the evanescent acoustic field through the phononic waveguide coupling or by direct IDT excitation. These waveguide and resonator structures will be basic elements in future phononic integrated circuits of both fundamental and practical interests<sup>56,71</sup>.

## II. WAVEGUIDE

Efficient confinement and guiding of phonons is essential for scalable operation of phononic devices. In the past decades, SAW has been mostly employed in applications that utilize its vertical confinement at the surface of substrates. However, the lateral confinement to the

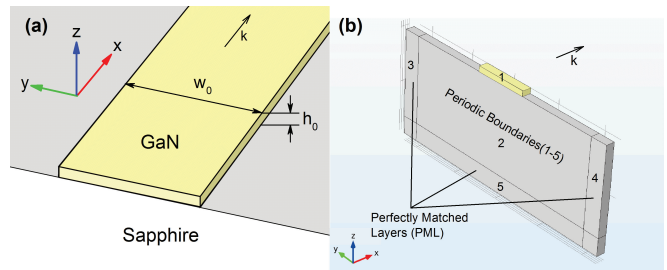


FIG. 1. (a) Schematic illustration of an unsuspended strip phononic waveguide.  $w_0$  and  $h_0$  represent the width and height of the GaN strip, respectively. (b) The geometry setup in COMSOL simulation. The phononic waveguide modes propagating in the uniform structure along  $\vec{x}$  with wavevector  $\vec{k}$  are calculated by applying a periodic boundary condition, and PMLs are employed to absorb radiative acoustic waves in substrate.

SAW is seldom studied. Alternatively, three-dimensional confinement of phonon has been mostly achieved in suspended phononic microstructures, which imposes practical constraints in fabrication yield and structural robustness. Here, we numerically study a phononic architecture based on unsuspended phononic waveguides and resonators. Shown in Fig. 1(a) is a typical strip waveguide. The basic requirement for phonon confinement is that the speeds of both transverse and longitudinal waves in strip material are slower than those in the substrate<sup>24</sup>. Thus, we choose the material platform of GaN-on-Sapphire satisfying these requirements, with parameters shown in Table II. An equivalent condition is also drawn in Ref. <sup>72</sup> where the waveguide layer material needs to be heavier and less stiff. More detailed analyses about the requirements for the existence of Love wave can be found in Ref. <sup>72–74</sup>.

Conventional Rayleigh waves have been widely studied and applied in SAW devices, while half-space single medium also supports shear-horizontal (SH) waves. In layered systems, in addition to layered Rayleigh waves, there are also Love waves<sup>57</sup>, which is first discovered by A.E.H. Love<sup>75</sup>. Love waves have a shear component with displacements in the surface, which can be regarded as modified forms of the SH wave. SH waves and Love waves are now attracting interests in spin-orbit interactions of phonons<sup>56</sup> and sensing applications<sup>47,58</sup>.

The basic properties of confined guiding modes are studied numerically by three-dimensional finite-element method (COMSOL Multiphysics v5.2). The waveguide geometrical parameters, namely its width  $w_0$  and height  $h_0$  marked in Fig. 1(a), determine the properties of the waveguide modes such as frequency, confinement, loss, and energy distributions. In this paper, all the simulations are carried out using periodic boundary conditions according to the translational symmetry of the structure, and perfectly matched layers (PMLs) are employed for studying the radiative loss, with the detailed numerical model illustrated in Fig. 1(b). To reveal the basic behav-

Material	GaN <sup>66,76</sup>	Sapphire <sup>77</sup>
Density ( $\text{g} \cdot \text{cm}^{-3}$ )	6.15	3.98
Young's modulus (GPa)	305	345
Poisson ratio	0.183	0.29
Longitudinal wave speed (m/s)	7350.0	10658.0
Transverse wave speed (m/s)	4578.3	5796.4

TABLE II. Elastic properties of GaN and Sapphire used in the simulation.

iors of the phononic waveguides, the anisotropy of GaN and sapphire are neglected.

Shown in Figs. 2(a)-(h) are fundamental to higher-order transverse phonon modes supported in a strip waveguide, with its width set at  $w_0 = 5 \mu\text{m}$  (for mode  $h$ ,  $w_0 = 6 \mu\text{m}$  because it doesn't appear at  $w_0 = 5 \mu\text{m}$ ) and  $h_0 = 0.5 \mu\text{m}$ . Wavelength along propagating direction is set at  $\lambda = 2 \mu\text{m}$ . The color mappings show the strength of normalized displacement  $|\vec{x}| / \max(|\vec{x}|)$  in each mode profile, which applies to all other figures of displacement field in this paper. Note that we label the modes by the corresponding characters  $a, \dots, h$  in the following for analyzing the evolution of mode profiles against geometry parameters. Mode  $a$  (Fig. 2(a)) is dominated by out-of-plane ( $z$ -direction) displacement, which we refer as quasi-Rayleigh mode owing to its reminiscence of Rayleigh wave<sup>78</sup>. Mode  $b$  has dominant in-plane ( $y$ -direction) motion and is a quasi-Love mode because of its similarity to Love wave<sup>75</sup>. The modes  $a$  and  $b$  can be regarded as the fundamental phononic modes in the strip with different polarizations ( $z$ - and  $y$ -polarized motion). Due to the lateral confinement and the edges, we found that the phononic modes are distinct from SAW modes. On one hand, the modes do not show pure flexural wave or in-plane shear waves. Especially, at the edge, it is difficult to identify the mode orientation because of the strong hybridization of deformation in all three orthogonal directions. On the other hand, higher-order transverse modes appear due to the lateral confinement (Figs. 2(c)-(h)). For example, compared to fundamental mode  $a$  and  $b$ , in which vibrations on the strip edges are in-phase, the motion of mode  $c$  and  $d$  on the opposite edges are out-of-phase. In the rest of this paper, we call the symmetric (in-phase) mode  $a$  as S-Rayleigh mode and call the anti-symmetric (out-of-phase) mode  $c$  as A-Rayleigh mode, as well as A-Love mode  $b$  and S-Love mode  $d$ . We also observe that higher-order modes (Figs. 2(e)-(h)) exhibit more complex field distributions.

For most applications, the concerned properties of guided phonon modes are<sup>24</sup>: dispersion, confinement, radiation loss, energy distributions. Therefore, we numerically evaluate the following properties with varying waveguide geometrical parameters.

1. Mode frequency  $f$  for a given wavelength  $\lambda$  or wavenumber  $k_x = 2\pi/\lambda$  along guided direction.
2. Phase velocity  $v_p = 2\pi f/k_x$  and group velocity

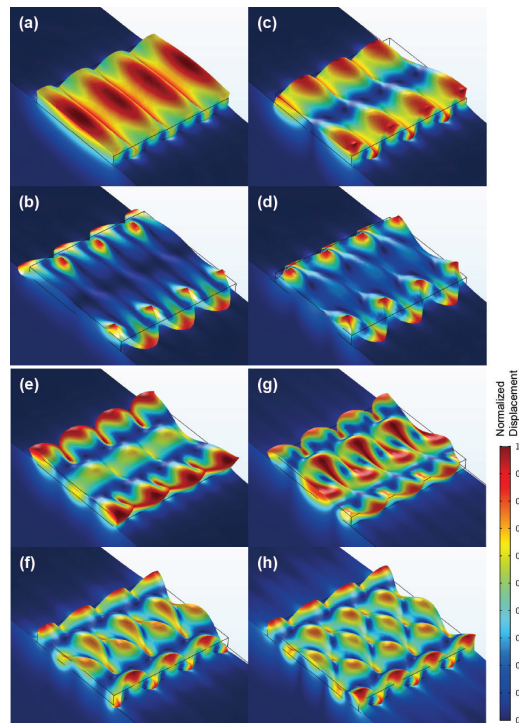


FIG. 2. Simulated displacement field profile for low-order phonon modes supported in an unsuspended strip waveguide. The color mappings show the strength of displacements  $|\vec{x}|$  normalized by their own maximum  $\max(|\vec{x}|)$ , which applies to all other figures of displacement field in this paper. Displacement amplitude is internally excited by the simulation software, so only relative strength  $|\vec{x}| / \max(|\vec{x}|)$  has significance.  $\max(|\vec{x}|)$  is extracted among the entire field of each mode, and every following figure is normalized to their own maximum. But since the color map setups are the same, we let them share one common color bar for simplicity. (a) Symmetric quasi-Rayleigh mode  $a$ . (b) Anti-symmetric quasi-Love mode  $b$ . (c) Anti-symmetric quasi-Rayleigh mode  $c$ . (d) Symmetric quasi-Love mode  $d$ . (e)-(h) Higher-order phonon modes  $e$ - $h$ . The italic characters label different modes and will be used throughout this paper. Wavelength  $\lambda$  along guided direction  $x$  are all set at  $2 \mu\text{m}$ . The waveguide height is fixed at  $h_0 = 0.5 \mu\text{m}$  while its width is set at  $w_0 = 5 \mu\text{m}$  except that the  $w_0$  of mode  $h$  is chosen to be  $6 \mu\text{m}$  because that specific mode does not appear for  $w_0 = 5 \mu\text{m}$ .

$$v_g = 2\pi df/dk_x.$$

### 3. Mode area

$$A_{\text{eff}} = \frac{1}{L} \frac{\iiint W(x, y, z) dx dy dz}{\max(W(x, y, z))} \quad (1)$$

where  $L$  is the waveguide length along the propagation direction,  $W(x, y, z)$  is the elastic strain energy density. The integral and maximum are calculated in the full simulated region. The mode area is a concept borrowed from photonics (see Ref. 79,80) as a measure of lateral confinement, where a smaller  $A_{\text{eff}}$  indicates stronger confinement of phonon.

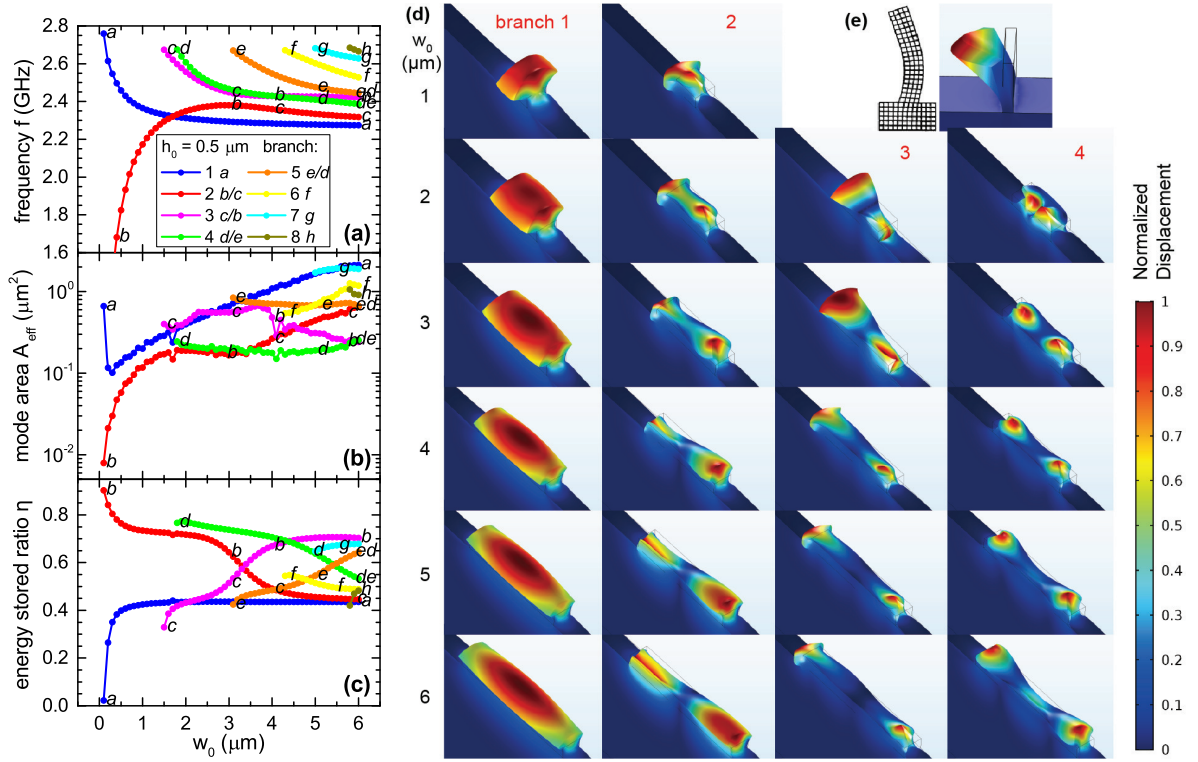


FIG. 3. Properties of phononic modes in a strip waveguide as the waveguide width  $w_0$  is varied. (a)-(c) Frequency  $f$ , mode area  $A_{eff}$ , and energy confinement ratio  $\eta$ , versus  $w_0$ , respectively. (d) Evolution of mode hybridizations when  $w_0$  is varied with an increment of  $1 \mu\text{m}$ . The color mappings show the strength of normalized displacement  $|\vec{x}|/\max(|\vec{x}|)$  in each mode profile. Note the  $\max(|\vec{x}|)$  is selected among all displacement field images for each mode, or equivalently, each column which plots one common mode has the same normalization. Among different columns, they use a common color mapping but their normalizations are distinct. (e) The deformation of anti-symmetrical flexural Lamb wave (left) and the simulation result (right) for a waveguide with an aspect ratio  $w_0/h_0 = 0.2$ .

#### 4. Quality factor

$$Q = 2\pi f \times \frac{\text{Energy stored}}{\text{Power loss}}. \quad (2)$$

In this paper, we only calculate the radiation loss into substrate. A discussion of other loss mechanisms can be found in the conclusion Sec. VI.

#### 5. Energy confinement ratio

$$\eta = \frac{\iiint_{\text{strip}} W(x, y, z) dx dy dz}{\iiint_{\text{all}} W(x, y, z) dx dy dz} \quad (3)$$

indicates the ratio between elastic strain energy stored in the phononic waveguide and the total elastic strain energy.

Figures 3(a)-(c) show the modal frequency ( $f$ ), area ( $A_{eff}$ ), and energy storage ratio ( $\eta$ ) of 8 phonon modes versus the width  $w_0$  of strip waveguide, with a fixed height  $h_0 = 0.5 \mu\text{m}$  and wavelength along propagation direction  $\lambda = 2 \mu\text{m}$ . To clarify complicated mode hybridization, we now explain the notations and colors of plots that are adopted in this paper. By varying the

waveguide geometry by small increments, the mode properties vary smoothly, thus we can track the frequencies or other parameters as continuous curves, which is called “branch” and labeled by different colors. As shown in the frequency plot (Fig. 3(a)), each branch is assigned with one specific color consistent with all other properties plots. As explained above, due to the strong mode hybridization in the strip waveguides, it is very difficult to identify mode orders or polarizations by branches. Therefore, we only label the modes in the regime that can be clearly distinguished according to the modes shown in Fig. 2. Sections labeled with two characters indicate the modes are experiencing hybridization.

The model frequency features versus width  $w_0$ , as shown in Fig. 3(a), indicates a transition between single-mode and multi-mode waveguide. At large  $w_0$  values, all phonon mode branches asymptotically approach slab phonon modes in GaN-on-sapphire thin films. When  $w_0$  becomes comparable to  $\lambda$ , the curves branch off and the behaviors of each branch can be explained as follows. Since the lateral confinement imposes an approximate quantization condition  $k_y \sim \frac{n\pi}{w_0}$ , an increasing  $w_0$  results in a reduction of total phonon wavenumber as

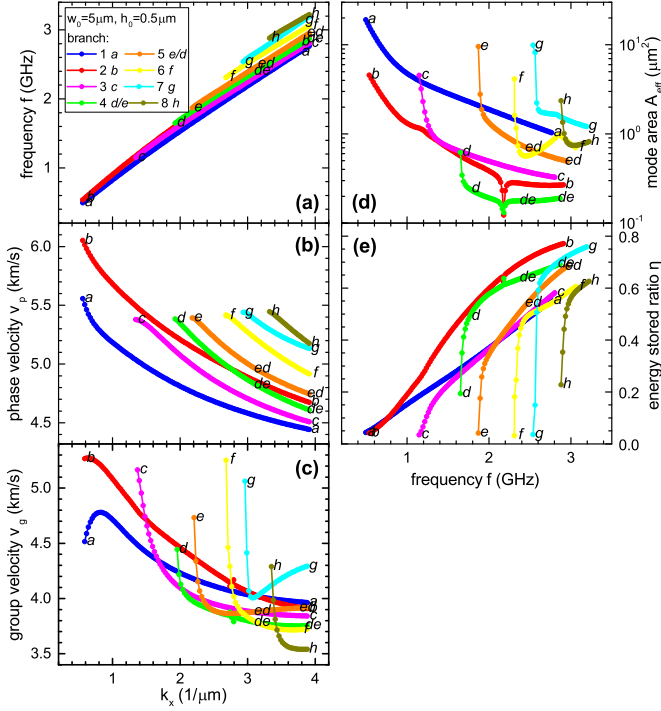


FIG. 4. Dispersion characteristics for phononic modes on strip waveguide, with geometry parameters  $w_0 = 5 \mu\text{m}$  and  $h_0 = 0.5 \mu\text{m}$  (aspect ratio  $w_0/h_0 = 10$ ). (a) Frequency  $f$  versus waveguide wavenumber  $k_x$ . (b) and (c) Phase velocity and group velocity versus  $k_x$ , respectively. (d) and (e) Mode area  $A_{eff}$  and energy confinement ratio  $\eta$  versus  $f$ , respectively.

$k = \sqrt{k_x^2 + k_y^2}$  for a fixed  $k_x$ , and hence a monotonic reduction of frequency approaching a constant. This intuitive interpretation is valid for most modes, however, fails for the A-Love modes  $b$ . According to the mode area and energy confinement ratio given in Figs. 3(b) and (c), the confinement of A-Love mode  $b$  is excellent at small  $w_0 \ll \lambda$  (rapid reducing of mode area), and thereby almost all wave energy is confined in the strip. It could be interpreted as the effective boundary becomes air-GaN for the A-Love mode  $b$  as opposed to sapphire-GaN for the other modes, and consequently, it can be treated as an anti-symmetrical flexural Lamb wave of a plate normal to  $y$  direction (Fig. 3(e))<sup>81</sup>. For a plate mode, the vibration frequency  $f \propto \sqrt{\frac{D}{\rho w_0}}$ , in which bending stiffness  $D = \frac{w_0^3 E}{12(1-\nu^3)}$ <sup>82</sup> ( $\rho$ ,  $E$ ,  $\nu$  are density, Young's modulus and Poisson ratio, respectively.). Thus the frequency of A-Love mode  $b$  scales with  $w_0$  and decreases for narrow waveguides.

The interactions between the phonon modes lead to crossings and avoided crossings in Figs. 3(a)-(c). For the avoided crossings, the corresponding mode area and energy confinement ratio show crossing behavior, indicating the coupling between modes and the mode hybridization at these device parameters. For the crossing in frequency, the coupling between modes is negligible, so the

changes in mode area and energy confinement ratio is not noticeable. Outside of the hybridization regimes, the confinement of quasi-Rayleigh modes ( $a$  and  $c$ ) weakens (larger mode area) with the increase of width, while that of quasi-Love modes ( $b$  and  $d$ ) remains relatively confined. At very small  $w_0$ , however, the waveguide becomes too narrow to support a fully confined mode  $a$ , and its mode frequency rapidly approaches its cutoff frequency which is the frequency of SAW in substrate for  $\lambda = 2 \mu\text{m}$ . The mode area of A-love mode  $b$ , in contrast to mode  $a$ , drops because this mode resembles anti-symmetrical flexural Lamb wave at small width, and its confinement is enhanced as width narrows<sup>81</sup> (like a vibrating membrane whose energy is tightly concentrated in the waveguide region thus the influence from substrate is negligible). The quasi-Love modes ( $b, d$ ) exhibit stronger confinement than quasi-Rayleigh modes' ( $a, c$ ) due to the much larger  $\eta$  of quasi-Love modes (except the hybridization regime), as shown in Fig. 3(c).

For a strip waveguide of fixed cross-section  $h_0 = 0.5 \mu\text{m}$  and  $w_0 = 5 \mu\text{m}$ , the dispersion characteristics shown in Fig. 4 are numerically calculated as a function of the mode wavenumber  $k_x$ . In Fig. 4(b), the quasi-Love modes  $b$  and  $d$  have faster phase velocities than their corresponding quasi-Rayleigh modes and their behaviors approach the infinite surface according to analytical predictions in Ref. 73,83,84. The cutoffs result in sharp rising of group velocities in Fig. 4(c) at small wavevectors, and meanwhile, in Fig. 4(d), mode areas rise sharply at low frequencies, indicating a remarkable divergence of the confinement when the size of strip becomes much smaller than the wavelength. This is confirmed in Fig. 4(e) that energy confinement ratio decreases, i.e. phonon energy spreads into the substrate, at small  $k_x$ . In Fig. 4(d), we also found an interesting minimum point of mode area that occur simultaneously for branches of mode  $b$  and  $d$  around 2.2 GHz. A close comparison with results in Figs. 4(a) and (b) reveals that these minima occur at the avoided crossing point of modes  $b$  and  $d$  when they are maximally hybridized. Therefore, the mode hybridization presents an unique approach to engineer the phononic modes and might find interesting phononic sensing applications.

### III. RING RESONATOR

In this section, we study the properties of ring resonators formed by bending and closing strip waveguide which supports phononic WGMs. The pioneering works of the acoustic WGMs date back to the discovery by Lord Rayleigh<sup>85,86</sup>, who reported the sound wave travels around a concave boundary in St Paul's Cathedral due to the continuous total internal reflection. The concept is generalized to electromagnetic waves<sup>87-89</sup>, which holds unique characteristics of high Q-factors, small mode volumes, and the ease of fabrication<sup>90</sup>. These remarkable merits are also possessed by phononic WGMs according

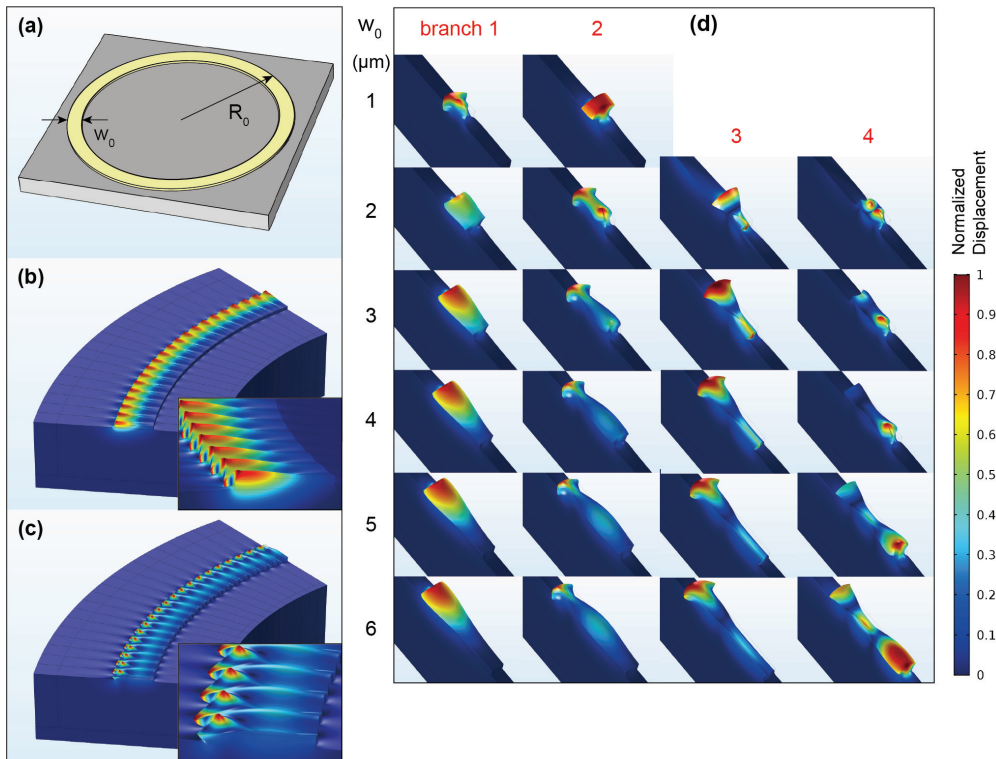


FIG. 5. (a) Schematic illustration of a strip ring resonator. (b) S-Rayleigh (mode  $a$ ) and (c) A-Love (mode  $b$ ) in ring resonator. The color mappings show the strength of normalized displacement  $|\vec{x}|/\max(|\vec{x}|)$  in each mode profile. (d) The evolution of mode hybridization profiles with varying  $w_0$ . The normalization convention is the same as we used in Fig. 3(d): the  $\max(|\vec{x}|)$  is selected among all displacement field images for each mode, or equivalently, each column which plots one common mode has the same normalization. (b-d) share a common color bar.

to our investigations.

Due to the cylindrical symmetry of the ring resonator, the eigenmode profiles of the elastic differential characteristic equation are in the form as  $u(r, z, \phi) = \psi(r, z)e^{im\phi}$ , where  $(r, z, \phi)$  are the cylindrical coordinators,  $\psi(r, z)$  is the field distribution at the cross-section,  $m$  is the angular momentum number. Utilizing the symmetry, we can numerically solve the mode profiles of a sector unit in  $\phi$  direction in COMSOL, with periodic boundary condition:  $u(r, z, \phi) = u(r, z, 0)e^{-im\phi}$ , where  $m = 2\pi R/\lambda$  for an azimuthal wavelength  $\lambda = 2\mu\text{m}$  along tangent direction.

Figures 5 (b) and (c) display the typical quasi-Rayleigh and quasi-Love WGMs in a ring resonator. Compared to those in waveguide (Figs. 2(a)-(b)), the displacement fields of WGMs in the ring are more concentrated at the outer rim. Figure 5(d) shows the mode profiles of the first four branches in Fig. 6(a). In the rest of this section, except for dispersion behaviors, we study the properties of WGMs around fixed geometry parameters  $\{R_0, w_0, h_0\} = \{50\mu\text{m}, 5\mu\text{m}, 0.5\mu\text{m}\}$ . Similar to the cases of strip waveguides, the colors of different branches are fixed in Figs. 6, 7, and 8. Instead of the mode area, the confinement in resonator is characterized by the mode

volume<sup>91</sup>,

$$V_{\text{eff}} = \frac{\iiint W(r, \theta, z) r dr d\theta dz}{\max[W(r, \theta, z)]}. \quad (4)$$

As shown in Fig. 6(a), the dependence of mode frequencies with respect to width  $w_0$  follows the same trend of those of strip waveguides [Fig. 3(a)]. However, comparing to the crossing in waveguide, there is avoided crossing between mode  $a$  and  $b$ , arising from the broken symmetry (hence mode hybridization) in the bending waveguide. The mode volume and energy confinement ratio  $\eta$  are presented in Figs. 6(b) and (d), showing similar crossing and avoid-crossing behavior as in the waveguide case.

For ring resonators, in contrast to the strip waveguides, there is always radiation loss due to the waveguide bending, and thus the  $Q$  factors of WGMs are finite. As shown in Fig. 6(c), S-Rayleigh  $a$ , A-Rayleigh  $c$  and A-Love  $b$  are three modes having the highest  $Q$  factors. For mode  $a$  and  $b$ ,  $Q$ s are sensitive to the width at small  $w_0$  value but almost constant when  $w_0$  exceeds  $3\mu\text{m}$ , implying a saturation of loss approaching the case of a disk resonator. We observe an abrupt increment of  $Q$  when  $b$  and  $a$  are hybridized at around  $w_0 = 1.7\mu\text{m}$ , suggesting that the mode  $b$  and  $a$  couple to a common leaky modes in substrate and their destructive interference suppresses the phonon loss. Thus the special width leads to a

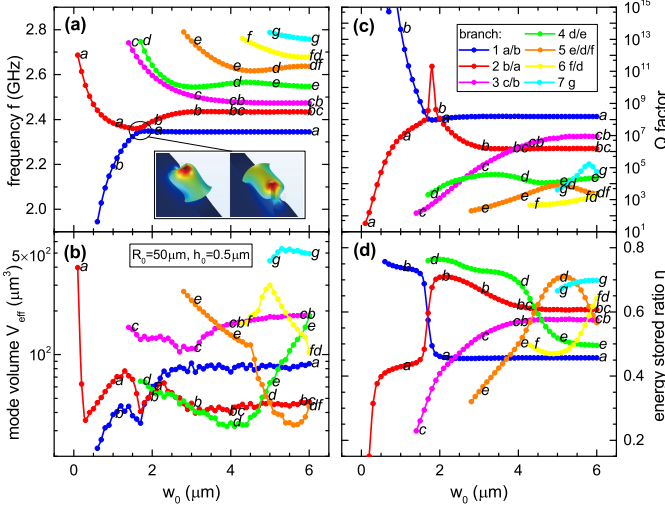


FIG. 6. Phononic mode properties in a ring resonator of varying width  $w_0$ . The ring radius and height are fixed respectively at  $R_0 = 50 \mu\text{m}$  and  $h_0 = 0.5 \mu\text{m}$ . (a)-(d) show frequency, mode volume  $V_{\text{eff}}$ ,  $Q$  factor, and energy confinement ratio  $\eta$ , respectively. The insets of (a) are the mode profiles of hybridized modes of (a, b) at  $w_0 = 1.7 \mu\text{m}$ .

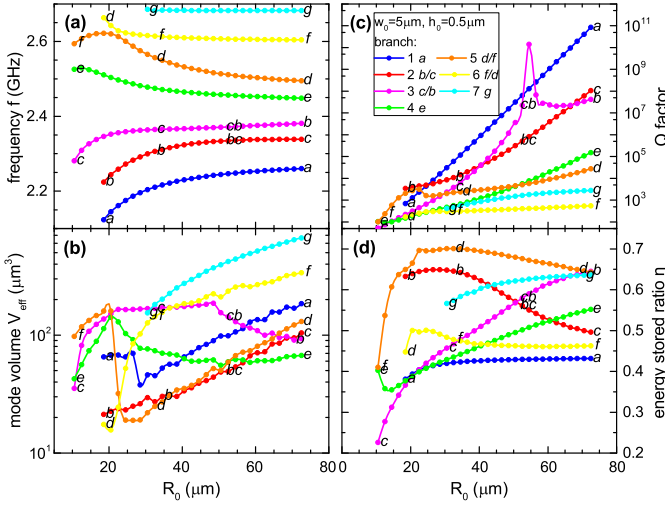


FIG. 7. Phononic mode properties in a ring resonator as functions of ring radius  $R_0$  with width  $w_0 = 5 \mu\text{m}$ , height  $h_0 = 0.5 \mu\text{m}$ . (a-d) show frequency, mode volume  $V_{\text{eff}}$ ,  $Q$  factor and energy confinement ratio  $\eta$ , respectively.

parameter-tuning type of bound state in continuum<sup>92,93</sup>.

Figure 7(a) shows the properties of phononic WGMs with varying radius. For a fixed  $\lambda$ , the frequencies of the ring converge to the case of straight waveguide at large  $R_0$  values with their calculated modal volumes shown in Figure 7(b). An optimal radius exists for each mode because the lateral confinement (i.e. effective mode area  $A_{\text{eff}}$ ) becomes better for larger  $R_0$ , while the mode volume is approximately proportional to  $R_0$  ( $V_{\text{eff}} \approx 2\pi R_0 A_{\text{eff}}$ ). The  $Q$  factors in Fig. 7(c) increase exponentially with increas-

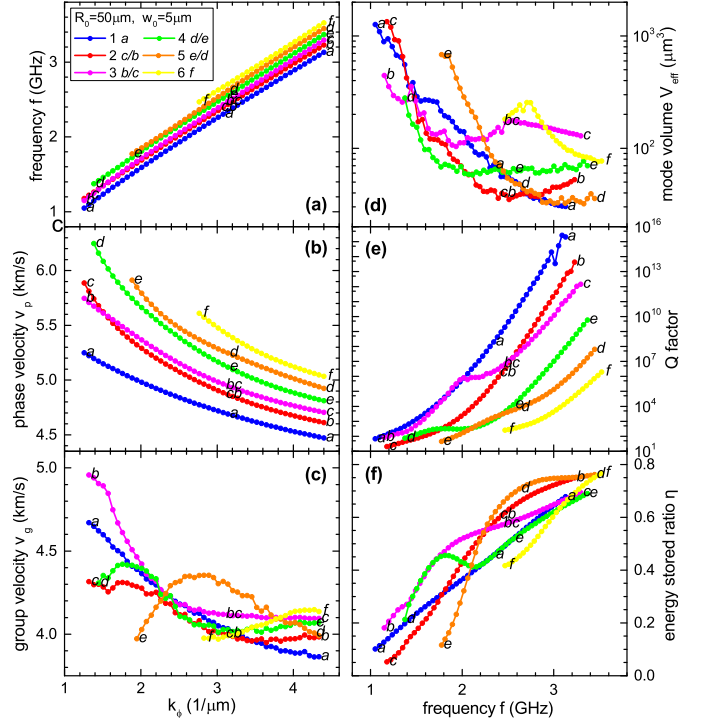


FIG. 8. Dispersion characteristics for modes in a ring resonator of radius  $R_0 = 50 \mu\text{m}$ , width  $w_0 = 5 \mu\text{m}$ , and height  $h_0 = 0.5 \mu\text{m}$ . (a) Modal frequencies  $f$  versus  $k_\phi$ —the effective propagating wavenumber defined as  $m/R_0$ , with  $m$  is angular momentum number. (b) and (c) Phase velocity and group velocity versus  $k_\phi$ . (d-f) Mode volume  $V_{\text{eff}}$ ,  $Q$  factor, and energy confinement ratio  $\eta$  versus  $f$ , respectively.

ing  $R_0$ , indicating radiation loss to the substrate caused by bending decreases exponentially with the curvature, similar to the radiation loss of optical WGM in dielectric spheres<sup>87,91</sup>. The increment of  $Q$  when  $b$  and  $c$  are hybridized at around  $R_0 = 54 \mu\text{m}$  can be explained with the same reason as that of  $b$  and  $a$  in Fig. 6(c).

The dispersion characteristics of ring resonator are summarized in Fig. 8. The  $k_\phi = m/R_0$  in the figure is effective propagating wavenumber along tangential direction. Most branches resemble their counterparts in the strip waveguide (Fig. 4), including  $f - k_\phi$  relation, and the decrease of phase velocity and mode volume, and increase of ratio  $\eta$  with increasing  $k_\phi$  or  $f$ . We also compute  $Q$  factors which grow exponentially at short wavelengths.

#### IV. DIRECTIONAL COUPLER

In an integrated phononic circuit, multiport devices transporting and routing phonons between components such as the waveguide-waveguide and waveguide-resonator coupler are indispensable circuit elements. A directional coupler consists of two closely placed parallel waveguides. Here we study the phononic coupling through the coupled-mode theory by analogy to

its optical counterpart widely used in the photonic community<sup>94–96</sup>. The coupling between the modes in different waveguides arises from the tunneling of the elastic wave between them. The confined waveguide mode has a non-zero evanescent field that overlaps with the other waveguide, leading energy transfer in between.

The spatial mode amplitude evolution along the propagation direction in coupled waveguides for a given input signal frequency are described by the following equations

$$\frac{d}{dz}\alpha_1(z) = -ik_1\alpha_1(z) - ig_{12}\alpha_2(z), \quad (5)$$

$$\frac{d}{dz}\alpha_2(z) = -ik_2\alpha_2(z) - ig_{21}\alpha_1(z). \quad (6)$$

Here, the subscript “1”, “2” represent waveguide 1 (width  $w_1$ ) and 2 (width  $w_2$ ),  $k_{1(2)}$  is the wavenumber of the mode in waveguide 1(2), and  $g_{12}$ ,  $g_{21}$  are the coupling coefficients between two modes. For lossless waveguides, coefficient  $g$  must satisfy  $g_{12} = g_{21}^*$  due to the power conservation<sup>96</sup>. Setting  $g_{12}g_{21} = |g|^2$  and solving Eqs. (5) and (6), we obtain the wavenumber eigenvalues of

$$k_{\pm} = \frac{k_1 + k_2}{2} \pm \sqrt{\left(\frac{k_1 - k_2}{2}\right)^2 + |g|^2} \quad (7)$$

for hybrid modes in two waveguides. When  $k_1 = k_2 = k$ , the difference between  $k_{\pm}$  reaches the minimum  $2|g|$ , and the eigenmodes are the  $a_1 \pm a_2$ , as an equal superposition of two waveguide modes. If the phonon input at the first waveguide with  $a_1(0) = 1$  and  $a_2(0) = 0$ , we arrive at

$$\alpha_1(z) = \cos(|g|z) e^{-ikz}, \quad (8)$$

$$\alpha_2(z) = \sin(|g|z) e^{-i(kz + \frac{\pi}{2})}. \quad (9)$$

Thus, the phonons in the first waveguide  $\alpha_1$  could be fully transported into the second waveguide  $\alpha_2$  after a coupling distance of  $\pi/2|g|$ , or half of the phonons can be transmitted into mode  $\alpha_2$  after a coupling distance  $\pi/4|g|$ . The larger the  $|g|$ , the quicker the energy exchanges.

### A. Coupling between two identical waveguides

For two identical waveguides with  $w_1 = w_2$ , the wavenumbers of the modes are the same ( $k_1 = k_2$ ), thus all supported modes can couple between the two waveguides without phase mismatching. Here, we set the width  $w_0 = 5 \mu\text{m}$  and height  $h_0 = 0.5 \mu\text{m}$  for both waveguides, as shown in Fig. 9(a). From the analysis above, we can estimate the coupling strength  $g$  between two waveguides by the splitting of  $k_{\pm}$ .

Figure 9(b) shows the coupling strength of various waveguide modes with different gap, where the label  $a-g$  corresponds to the modes introduced in Fig. 3. We set the  $\lambda = 2 \mu\text{m}$ . Eigenmodes  $a$ ,  $b$  and  $c$  in the coupled waveguides are shown in Fig. 9(c), featuring in-phase

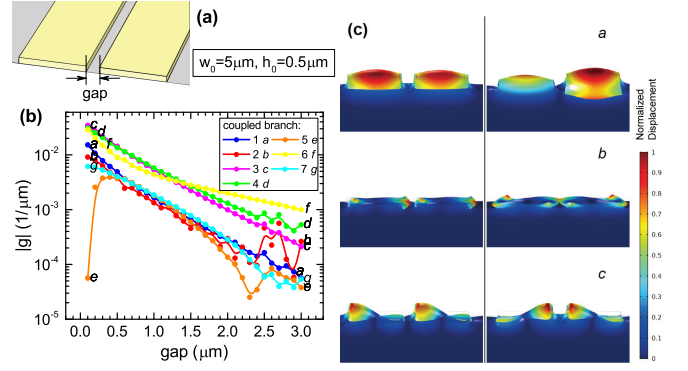


FIG. 9. (a) Schematic of the directional coupler. (b) The estimated coupling strengths  $|g|$  as a function of  $gap$ . Set the  $\lambda = 2 \mu\text{m}$  along guided direction. (c) The displacement field profiles for the in-phase and out-of-phase modes in the directional coupler, which is made by two identical waveguides with  $gap = 5 \mu\text{m}$ . The color mappings show the strength of normalized displacement  $|\vec{x}|/\max(|\vec{x}|)$  in each profile. The in-phase and out-of-phase figures share the same normalization, and all figures share the common color bar.

and out-of-phase hybridized modes in the coupled waveguides as predicted by the coupled-mode theory. Since the evanescent field exponentially decays with the distance to the waveguide, a reduction of the  $g$  with increasing gap is expected. As shown by the numerical simulations, there is a clear exponential relation between the coupling strength and the gap, yet the trends of high order modes  $e$  and  $f$  slightly deviate from the exponential curve at small/large gaps. This can be attributed to the weaker confinement of the high order modes, for which the perturbative approximation in coupled-mode theory is no longer accurate.

### B. Coupling between dissimilar waveguides

The coupled-mode theory is also applicable to dissimilar modes in dissimilar waveguides, therefore opens the possibility for mode conversions with different polarization or mode orders as long as there is a finite mode overlap between them. From Eq. 6, the maximum ratio of energy transmittance between the two modes is  $\text{sinc}^2[1 + (k_1 - k_2)^2/4g^2]^{1/2}$ . Thus, for efficient energy transfer, we should adjust waveguide width to match the wavenumber of the two dissimilar modes, i.e. fulfill the phase-matching condition. In Fig. 10(a), the width of one waveguide ( $w_1$ ) is changed while the width of the other is fixed ( $w_2 = 4.5 \mu\text{m}$ ) in order to meet with the phase-matching condition

$$k_1(w_1) = k_2(w_2) \quad (10)$$

The modal frequencies of coupled waveguides are shown in Fig. 10(a) as the  $w_1$  is varied from  $1 \mu\text{m}$  to  $2.5 \mu\text{m}$ . From the plot, we observe four avoid crossings, corresponding to four regions of modal coupling: I : ( $b_1, a_2$ ),

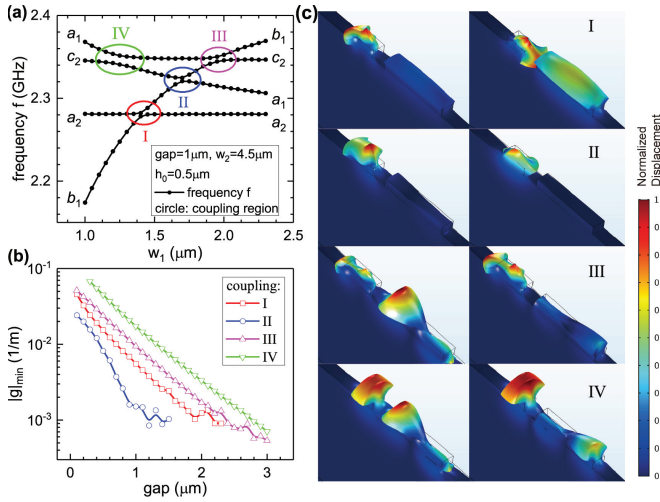


FIG. 10. (a) Modal frequencies in directional coupler of dissimilar waveguides, plotted against the waveguide width  $w_1$ , with the other waveguide width and coupling gap fixed ( $w_2 = 4.5 \mu\text{m}$ ,  $\text{gap} = 1 \mu\text{m}$ ). Due to the modal coupling, four avoided-crossing regions {I, II, III, IV} are observed when the frequencies of modes in separate waveguides approach each other. The subscripts of waveguide mode labels {1, 2} denote the waveguide 1 and 2 respectively. (b) The modal coupling strength  $|g|$  as a function of  $\text{gap}$ . (c) The mode profiles of the directional coupler in the four avoided crossing regions. The color mappings show the strength of normalized displacement  $|\vec{x}|/\max(|\vec{x}|)$  in each profile. The in-phase and out-of-phase figures share the same normalization, and all figures share the common color bar.

II:  $(a_1, b_1)$ , III:  $(b_1, c_2)$ , IV:  $(a_1, c_2)$ . Fig. 10(c) displays the displacement fields of the four coupling regions at the minimum frequency differences. Similar to the identical waveguides,  $g$  values of different modes also exhibit an exponential dependency on  $\text{gap}$  (Fig. 10(b)). Among four cases, coupling II is particularly interesting because it represents a special mechanism of “self coupling” between mode  $a$  and  $b$  within waveguide 1, corresponding to a double tunneling process that mode  $a$  and mode  $b$  in waveguide 1 both couple to waveguide 2, which mediates the coupling of mode  $a$  and  $b$ . The double tunneling mechanism could also explain the much faster decaying of the coupling strength for case II. With such a mechanism, we would expect the realization of a single-waveguide mode converter<sup>97</sup> in the future with the assistance of an ancillary waveguide.

## V. COUPLING TO IDT

Aside from the vibrational properties of phononic waveguides and ring resonators, the excitation and detection of phonons are also of practical importance and interests, for example, in phononic implementation of microwave delay lines and filters. Based on the model of ring resonator presented in Sec. III, we add

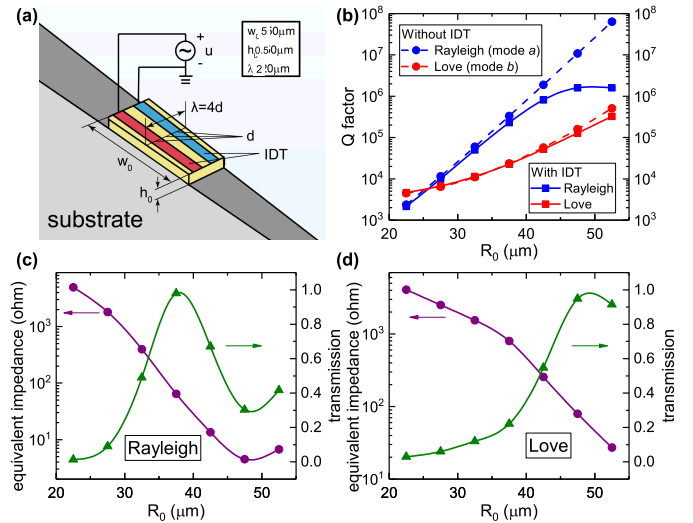


FIG. 11. (a) Schematic illustration of the IDT integrated ring resonator, with the electrodes of IDTs connected to external microwave cable (not shown) for signal input. (b) The influence of the IDT on the mode  $Q$  factors. (c) and (d) The equivalent impedance and the energy transmission (conversion efficiency) from microwave to phonon as functions of the ring radius for S-Rayleigh and A-Love modes, respectively.

IDT electrodes on the top surface of the ring resonator (Fig. 11(a)), and numerically investigate the coupling between IDT and phononic ring resonators and its efficiency to excite phonons. In this model, only the electrical effect of the IDT electrodes to the resonator is considered, while the mechanical and other effects due to loading of the electrodes are ignored (such as mass loading).

We first evaluate the quality factor of the mechanical ring resonator under the presence of IDT electrodes. The width of each electrode is  $1/4$  of the acoustic wavelength and the electrodes cover half of the ring resonator area. For the S-Rayleigh mode  $a$  with wavelength of  $2 \mu\text{m}$  in a  $5 \mu\text{m}$ -wide ring resonator without IDT, the quality factor increases exponentially with the radius of the resonator as the quality factor is limited by the radiation loss; with the IDT electrodes, the quality factor saturates when the radius is larger than  $40 \mu\text{m}$ , as shown in Fig. 11(b). The presence of the electrodes modifies the local phonon velocity, due to the  $\delta v/v$  effect<sup>70</sup>. Hence, the IDTs break the cylindrical symmetry of the perfect ring, leading to extra coupling of the phonon mode in ring to the leaky phonon modes in the bulk substrate. The same effect also happens to the Love mode. When the radius is small and radiation loss is dominant, the quality factors with and without IDT electrodes are almost the same. At larger radius in our simulation, the IDT electrodes induced loss becomes comparable with radiation loss and the quality factor with IDT electrodes are slightly lower.

To evaluate the external coupling to the phonon resonator, we also simulate the equivalent impedance of the IDT coupled mechanical ring resonator in order to achieve impedance matching to  $Z_0 = 50 \Omega$  transmission

lines for maximal acoustic launching efficiency. In the COMSOL simulation, by assigning voltage  $V$  on the electrodes and measuring the current flow  $I$  on the electrodes at mechanical resonance frequency, the equivalent impedance,  $Z = V/I$ , can be extracted. The microwave reflectivity can be expressed by

$$r = \frac{Z - Z_0}{Z + Z_0} \quad (11)$$

and the corresponding microwave to mechanical energy conversion efficiency  $T = 1 - |r|^2$ . The simulated results are plotted in Fig. 11(c) and (d) for quasi-Rayleigh and quasi-Love mode, respectively. The results indicate that the effective impedance of the IDT coupled mechanical resonator decreases exponentially with the radius and the impedance matching condition  $Z = Z_0$  can be satisfied with a certain radius, which gives 100% microwave-to-phonon conversion efficiency. To explain the dependence of the impedance on the radius, we consider the Butterworth-Van Dyke circuit model of the piezomechanical resonator which consists of a static capacitance  $C_0$  in parallel with a motional series RLC circuit. The admittance of the circuit is<sup>98</sup>

$$\begin{aligned} Y(\omega) &= -i\omega C_0 + \frac{1}{1/(-i\omega C_m) - i\omega L_m + R_m} \\ &= -i\omega C_0 + i\omega_s^2 C_m \frac{\omega}{\omega^2 + i\omega_s\omega/Q_i - \omega_s^2} \\ &= -i\omega C_0 + \frac{iC_m\omega_s^2\omega(\omega^2 - \omega_s^2)}{(\omega^2 - \omega_s^2)^2 + \omega_s^2\omega^2/Q_i^2} \\ &\quad + \frac{\omega_s^3\omega^2 C_m/Q_i}{(\omega^2 - \omega_s^2)^2 + \omega_s^2\omega^2/Q_i^2} \end{aligned} \quad (12)$$

where  $C_m$ ,  $L_m$  and  $R_m$  are the motional capacitance, inductance and resistance. The mechanical resonance  $\omega_s = 1/\sqrt{L_m C_m}$  and its intrinsic quality factor  $Q_i = 1/\omega_s R_m C_m$ . Note that  $\omega_s$  is the resonant frequency without the presence of the IDT electrodes, and suppose that with IDT on it, the resonant frequency is  $\omega_f$ . This resonant frequency shift originates from the  $\delta v/v$  effect and the value  $(\omega_f - \omega_s)/\omega_s$  equals  $\frac{1}{2}\delta v/v$  (as the electrodes cover only half of the ring resonator). In the regime where the quality factor is limited by intrinsic radiation loss instead of the  $\delta v/v$  scattering, we have  $(\omega_f - \omega_s)/\omega_s = \delta v/v \ll 1/Q_i$ . In this case, the admittance can be simplified to

$$Y(\omega_f) = -i\omega_f C_0 + \omega_f C_m Q_i \quad (13)$$

with the real part being dominant, we get the relation between the equivalent impedance and its quality factor

$$Z(\omega_f) = \frac{1}{\omega_f C_m Q_i} \quad (14)$$

We see that the equivalent impedance is inversely proportional to its quality factor. The motional capacitance  $C_m$  is proportional to the electrode area like  $C_0$ <sup>99</sup>, so it

is linearly proportional to the radius as the surface area increases while the quality factor increases exponentially with radius. So in Fig. 11(c) and (d), the impedance's dependence with radius is mostly exponential, consistent with the quality factor simulated in Fig. 11(b). The microwave-to-phonon conversion efficiency can also be understood from coupling condition point of view where the external coupling between the electrodes and the resonator is weak, but by changing the resonator's intrinsic energy decay rate, critical coupling condition can be satisfied and all the microwave energy can be converted into mechanical energy.

Therefore, the IDT integrated mechanical resonator can enhance microwave-phonon conversion efficiency, boost the performances of applications that require high excitation and collection efficiency and provide coherent interface between phononic and superconducting circuits.

## VI. CONCLUSION

In conclusion, we have quantitatively studied phononic mode properties in unsuspended strip waveguides and ring resonators. Our numerical results demonstrate efficient confinement of phonon in the practical GaN-on-sapphire microstructures, which provide a scalable platform of phononic integrated circuits for acoustic signal processing and enhanced phonon-matter or phonon-light interactions. Basic components for a phononic circuit are thoroughly investigated, including the directional coupler made by two waveguides, quasi-Rayleigh mode to quasi-Love mode conversion in coupled non-identical waveguides, ring resonator, as well as microwave photon-to-phonon conversion for efficient input and output coupling. It is worth noting that the studies in this paper can be generalized to other frequencies by rescaling the geometry parameters. For example, 10 GHz phononic waveguide modes could be realized with a thickness of 125 nm and a width of 500 nm, whose geometry is compatible with the photonic integrated circuits and promises the applications in optical Brillouin scattering.

Although not addressed in this paper, it is worth noting that there are various other loss mechanisms<sup>100</sup>. Some losses don't exist or can be neglected in our strip waveguide SAW devices, for example, our system doesn't use any suspended structures so it isn't subject to clamping or support losses. For the circuit damping caused by drive-and-detection circuit, we evaluate the equivalent impedance and  $Q$  factor in Sec. V. Scattering losses from crystal defects or thermal phonons are ignored, though thermoelastic damping can be one primary limits of the  $Q$  factors at room temperature. Recently, people has done phononic band structure engineering to reduce scattering of SAW into bulk modes<sup>41,46</sup>. However, scattering losses from surface roughness due to fabrication disorder, can be critical for miniaturizing phononic systems and thus for high-frequency application<sup>101</sup>, since the scattering loss coefficient has a quadratic dependency with respect

to the guided wave frequency<sup>102–104</sup>, it could be the main limitation to efficient photo-phonon interaction<sup>101,105</sup>. In addition, scaling to smaller geometry increases surface-to-volume ratios which may give rise to more surface loss, this loss mechanism has been found in other micromechanical systems<sup>106</sup>. Besides, we do not consider material losses due to any intrinsic microscopic processes. The damping from surrounding medium contributes to additional loss if the devices are operating under atmosphere or viscous medium.

We believe the phononic waveguides and ring resonators studied in this paper can be applied in future studies on phononic circuits<sup>107–109</sup>, gyroscopic sensors<sup>2,56,110</sup>, integrated acoustic-optics modulators<sup>12–15</sup>, circulators<sup>111</sup>, integrated delay line and data bus that communicates the quantum bits<sup>9</sup>.

## ACKNOWLEDGMENTS

This work was supported by DARPA/MTO's PRIGM: AIMS program through a grant from SPAWAR (N66001-16-1-4026). H.X.T. acknowledges funding support from Army Research Office (W911NF-18-1-0020) and Packard Fellowship in Science and Engineering. C.L.Z. thanks Liang Jiang for helpful discussions.

## DATA AVAILABILITY

The data that support the findings of this study are available from the corresponding author upon reasonable request.

- <sup>1</sup>C. Campbell, *Surface acoustic wave devices for mobile and wireless communications* (Academic press, 1998).
- <sup>2</sup>B. Y. Lao, "Gyroscopic Effect in Surface Acoustic Waves," *1980 Ultrason. Symp.*, 687 (1980).
- <sup>3</sup>J. Friend and L. Y. Yeo, "Microscale acoustofluidics: Microfluidics driven via acoustics and ultrasonics," *Rev. Mod. Phys.* **83**, 647 (2011).
- <sup>4</sup>C. K. Campbell, "Applications of surface acoustic and shallow bulk acoustic wave devices," *Proc. IEEE* **77**, 1453 (1989).
- <sup>5</sup>R. P. G. Mcneil, M. Kataoka, C. J. B. Ford, C. H. W. Barnes, D. Anderson, G. A. C. Jones, I. Farrer, and D. A. Ritchie, "On-demand single-electron transfer between distant quantum dots," *Nature* **477**, 439 (2011).
- <sup>6</sup>S. Hermelin, S. Takada, M. Yamamoto, S. Tarucha, A. D. Wieck, L. Saminadayar, C. Bäuerle, and T. Meunier, "Electrons surfing on a sound wave as a platform for quantum optics with flying electrons," *Nature* **477**, 435 (2011).
- <sup>7</sup>J. C. H. Chen, Y. Sato, R. Kosaka, M. Hashisaka, K. Muraki, and T. Fujisawa, "Enhanced electron-phonon coupling for a semiconductor charge qubit in a surface phonon cavity," *Sci. Rep.* **5**, 15176 (2015).
- <sup>8</sup>D. A. Golter, T. Oo, M. Amezcua, K. A. Stewart, and H. Wang, "Optomechanical Quantum Control of a Nitrogen-Vacancy Center in Diamond," *Phys. Rev. Lett.* **116**, 143602 (2016).
- <sup>9</sup>M. V. Gustafsson, T. Aref, A. F. Kockum, M. K. Ekstrom, G. Johansson, and P. Delsing, "Propagating phonons coupled to an artificial atom," *Science* **346**, 207 (2014).
- <sup>10</sup>K. J. Satzinger, Y. Zhong, H.-S. Chang, G. A. Peairs, A. Bienfait, M.-H. Chou, A. Cleland, C. R. Conner, É. Dumur, J. Grebel, *et al.*, "Quantum control of surface acoustic-wave phonons," *Nature* **563**, 661 (2018).
- <sup>11</sup>A. Bienfait, K. J. Satzinger, Y. Zhong, H.-S. Chang, M.-H. Chou, C. R. Conner, É. Dumur, J. Grebel, G. A. Peairs, R. G. Povey, *et al.*, "Phonon-mediated quantum state transfer and remote qubit entanglement," *Science* **364**, 368 (2019).
- <sup>12</sup>D. A. Fuhrmann, S. M. Thon, H. Kim, D. Bouwmeester, P. M. Petroff, A. Wixforth, and H. J. Krenner, "Dynamic modulation of photonic crystal nanocavities using gigahertz acoustic phonons," *Nat. Photonics* **5**, 605 (2011).
- <sup>13</sup>S. A. Tadesse and M. Li, "Sub-optical wavelength acoustic wave modulation of integrated photonic resonators at microwave frequencies," *Nat. Commun.* **5**, 5402 (2014).
- <sup>14</sup>H. L. I. Uan, S. E. A. T. Adesse, Q. I. Y. U. L. Iu, H. Li, S. A. Tadesse, Q. Liu, and M. Li, "Nanophotonic cavity optomechanics with propagating acoustic waves at frequencies up to 12 GHz," *Optica* **2**, 826 (2015).
- <sup>15</sup>S. A. Tadesse, H. Li, Q. Liu, and M. Li, "Acousto-optic modulation of a photonic crystal nanocavity with Lamb waves in microwave K band," *Appl. Phys. Lett.* **107** (2015), 10.1063/1.4935981.
- <sup>16</sup>G. Kurizki, P. Bertet, Y. Kubo, K. Mølmer, D. Petrosyan, P. Rabl, and J. Schmiedmayer, "Quantum technologies with hybrid systems," *Proc. Natl. Acad. Sci.* **112**, 3866 (2015).
- <sup>17</sup>M. J. A. Schuetz, E. M. Kessler, G. Giedke, L. M. K. Vandersypen, M. D. Lukin, and J. I. Cirac, "Universal Quantum Transducers Based on Surface Acoustic Waves," *Phys. Rev. X* **5**, 031031 (2015).
- <sup>18</sup>V. S. Shumeiko, "Quantum acousto-optic transducer for superconducting qubits," *Phys. Rev. A* **93**, 023838 (2016).
- <sup>19</sup>A. Clerk, K. Lehnert, P. Bertet, J. Petta, and Y. Nakamura, "Hybrid quantum systems with circuit quantum electrodynamics," *Nature Physics*, 1 (2020).
- <sup>20</sup>R. Manenti, A. F. Kockum, A. Patterson, T. Behrle, J. Rahamim, G. Tancredi, F. Nori, and P. J. Leek, "Circuit quantum acoustodynamics with surface acoustic waves," *Nature communications* **8**, 1 (2017).
- <sup>21</sup>B. A. Moores, L. R. Sletten, J. J. Viennot, and K. Lehnert, "Cavity quantum acoustic device in the multimode strong coupling regime," *Physical review letters* **120**, 227701 (2018).
- <sup>22</sup>A. Noguchi, R. Yamazaki, Y. Tabuchi, and Y. Nakamura, "Qubit-assisted transduction for a detection of surface acoustic waves near the quantum limit," *Physical review letters* **119**, 180505 (2017).
- <sup>23</sup>K. H. Yen, "Broadband Efficient Excitation of the Thin-Ribbon Waveguide for Surface Acoustic Waves," *Appl. Phys. Lett.* **20**, 284 (1972).
- <sup>24</sup>A. Oliner, "Waveguides for acoustic surface waves: A review," *Proc. IEEE* **64**, 615 (1976).
- <sup>25</sup>A. A. Oliner, "Waveguides for surface waves," in *Acoust. Surf. Waves* (Springer Berlin Heidelberg, 1978) pp. 187–223.
- <sup>26</sup>R. Knox and D. Owen, "Distributed Components in Microwave Elastic Surface Wave Circuits," in *G-MTT 1970 Int. Microw. Symp.*, Vol. 1 (IEEE, 1970) pp. 370–374.
- <sup>27</sup>F. Sandy and T. Parker, "Surface Acoustic Wave Ring Filter," in *1976 Ultrason. Symp.*, Vol. 79 (IEEE, 1976) pp. 391–396.
- <sup>28</sup>M. Goryachev, D. Creedon, E. Ivanov, S. Galliou, R. Bourquin, and M. Tobar, "Extremely high q-factor mechanical modes in quartz bulk acoustic wave resonators at millikelvin temperature," in *AIP Conference Proceedings*, Vol. 1633 (American Institute of Physics, 2014) pp. 90–92.
- <sup>29</sup>N. Carvalho, J. Bourhill, M. Goryachev, S. Galliou, and M. Tobar, "Piezo-optomechanical coupling of a 3d microwave resonator to a bulk acoustic wave crystalline resonator," *Applied Physics Letters* **115**, 211102 (2019).
- <sup>30</sup>S. V. Biryukov, G. Martin, and M. Wehnacht, "Ring waveguide resonator on surface acoustic waves," *Appl. Phys. Lett.* **90**, 173503 (2007).
- <sup>31</sup>S. V. Biryukov, H. Schmidt, A. V. Sotnikov, M. Wehnacht, T. Y. Chemekova, and Y. N. Makarov, "Ring waveguide res-

- onator on surface acoustic waves: First experiments,” *J. Appl. Phys.* **106**, 130 (2009).
- <sup>32</sup>A. Maznev, “Laser-generated surface acoustic waves in a ring-shaped waveguide resonator,” *Ultrasonics* **49**, 1 (2009).
- <sup>33</sup>R. Manenti, M. J. Peterer, A. Nersisyan, E. B. Magnusson, A. Patterson, and P. J. Leek, “Surface acoustic wave resonators in the quantum regime,” *Phys. Rev. B* **93**, 041411 (2016).
- <sup>34</sup>F. Liu, S. Peng, H. Jia, M. Ke, and Z. Liu, “Strongly localized acoustic surface waves propagating along a V-groove,” *Appl. Phys. Lett.* **94**, 2007 (2009).
- <sup>35</sup>P. Boucher, S. Rauwerdink, A. Tahraoui, C. Wenger, Y. Yamamoto, and P. V. Santos, “Ring waveguides for gigahertz acoustic waves on silicon,” *Appl. Phys. Lett.* **105**, 161904 (2014).
- <sup>36</sup>L. Fan, C.-L. Zou, M. Poot, R. Cheng, X. Guo, X. Han, and H. X. Tang, “Noise-free quantum optical frequency shifting driven by mechanics,” *arXiv preprint arXiv:1607.01823* (2016).
- <sup>37</sup>S. Mohammadi and A. Adibi, “On chip complex signal processing devices using coupled phononic crystal slab resonators and waveguides,” *AIP Advances* **1**, 041903 (2011).
- <sup>38</sup>R. N. Patel, Z. Wang, W. Jiang, C. J. Sarabalis, J. T. Hill, and A. H. Safavi-Naeini, “Single-mode phononic wire,” *Phys. Rev. Lett.* **121**, 040501 (2018).
- <sup>39</sup>K. Fang, M. H. Matheny, X. Luan, and O. Painter, “Optical transduction and routing of microwave phonons in cavity-optomechanical circuits,” *Nat. Photon.* **10**, 489 (2016).
- <sup>40</sup>D. Hatanaka, I. Mahboob, K. Onomitsu, and H. Yamaguchi, “Phonon waveguides for electromechanical circuits,” *Nat. Nanotech.* **9**, 520 (2014).
- <sup>41</sup>Y. Xu, W. Fu, C.-l. Zou, Z. Shen, and H. X. Tang, “High quality factor surface fabry-perot cavity of acoustic waves,” *Applied Physics Letters* **112**, 073505 (2018).
- <sup>42</sup>D. A. Golter, T. Oo, M. Amezcua, K. A. Stewart, and H. Wang, “Optomechanical Quantum Control of a Nitrogen-Vacancy Center in Diamond,” *Physical Review Letters* **116**, 143602 (2016).
- <sup>43</sup>C.-Y. Huang, J.-H. Sun, and T.-T. Wu, “A two-port ZnO/silicon Lamb wave resonator using phononic crystals,” *Applied Physics Letters* **97**, 031913 (2010).
- <sup>44</sup>E. B. Magnusson, B. H. Williams, R. Manenti, M.-S. Nam, A. Nersisyan, M. J. Peterer, A. Ardavan, and P. J. Leek, “Surface acoustic wave devices on bulk ZnO crystals at low temperature,” *Applied Physics Letters* **106**, 063509 (2015).
- <sup>45</sup>W. L. Ung, K. Mutaopoulos, P. Spink, R. W. Rambach, T. Franke, and D. A. Weitz, “Enhanced surface acoustic wave cell sorting by 3D microfluidic-chip design,” *Lab on a Chip* **17**, 4059 (2017).
- <sup>46</sup>L. Shao, S. Maity, L. Zheng, L. Wu, A. Shams-Ansari, Y.-I. Sohn, E. Puma, M. Gadalla, M. Zhang, C. Wang, E. Hu, K. Lai, and M. Loncar, “Phononic Band Structure Engineering for High-Q Gigahertz Surface Acoustic Wave Resonators on Lithium Niobate,” *Physical Review Applied* **12**, 014022 (2019).
- <sup>47</sup>C. Fu, A. J. Quan, J. T. Luo, H. F. Pang, Y. J. Guo, Q. Wu, W. P. Ng, X. T. Zu, and Y. Q. Fu, “Vertical jetting induced by shear horizontal leaky surface acoustic wave on 36° Y-X LiTaO<sub>3</sub>,” *Applied Physics Letters* **110**, 173501 (2017).
- <sup>48</sup>Y. Chu, P. Kharel, W. H. Renninger, L. D. Burkhardt, L. Frunzio, P. T. Rakich, and R. J. Schoelkopf, “Quantum acoustics with superconducting qubits,” *Science* **358**, 199 (2017).
- <sup>49</sup>T. Aubert, O. Elmazria, B. Assouar, L. Bouvot, and M. Oudich, “Surface acoustic wave devices based on AlN/sapphire structure for high temperature applications,” *Applied Physics Letters* **96**, 203503 (2010).
- <sup>50</sup>S. A. Tadesse and M. Li, “Sub-optical wavelength acoustic wave modulation of integrated photonic resonators at microwave frequencies,” *Nature Communications* **5**, 5402 (2014).
- <sup>51</sup>S. Fujii, T. Odawara, H. Yamada, T. Omori, K.-y. Hashimoto, H. Torii, H. Umezawa, and S. Shikata, “Low propagation loss in a one-port SAW resonator fabricated on single-crystal diamond for super-high-frequency applications,” *IEEE Transactions on Ultrasonics, Ferroelectrics, and Frequency Control* **60**, 986 (2013).
- <sup>52</sup>H. Okamoto, A. Gourgout, C.-Y. Chang, K. Onomitsu, I. Mahboob, E. Y. Chang, and H. Yamaguchi, “Coherent phonon manipulation in coupled mechanical resonators,” *Nature Physics* **9**, 480 (2013).
- <sup>53</sup>M. Metcalfe, S. M. Carr, A. Muller, G. S. Solomon, and J. Lawall, “Resolved Sideband Emission of  $\text{InAs}/\text{GaAs}$  Quantum Dots Strained by Surface Acoustic Waves,” *Physical Review Letters* **105**, 037401 (2010).
- <sup>54</sup>S. Valle, M. Singh, M. J. Cryan, M. Kuball, and K. C. Balar, “High frequency guided mode resonances in mass-loaded, thin film gallium nitride surface acoustic wave devices,” *Applied Physics Letters* **115**, 212104 (2019).
- <sup>55</sup>S. Wang, L. C. Popa, and D. Weinstein, “Tapered Phononic Crystal sawresonator in GaN,” in *2015 28th IEEE International Conference on Micro Electro Mechanical Systems (MEMS)* (2015) pp. 1028–1031.
- <sup>56</sup>W. Fu, Z. Shen, Y. Xu, C.-L. Zou, R. Cheng, X. Han, and H. X. Tang, “Phononic integrated circuitry and spin-orbit interaction of phonons,” *Nature communications* **10**, 1 (2019).
- <sup>57</sup>D. Morgan and E. Paige, “2 - acoustic waves in elastic solids,” in *Surface Acoustic Wave Filters (Second edition)*, Studies in Electrical and Electronic Engineering, edited by D. Morgan and E. Paige (Academic Press, Oxford, 2007) second edition ed., pp. 38 – 67.
- <sup>58</sup>H.-F. Pang, Y.-Q. Fu, Z.-J. Li, Y. Li, J.-Y. Ma, F. Placido, A. J. Walton, and X.-T. Zu, “Love mode surface acoustic wave ultraviolet sensor using ZnO films deposited on 36° Y-cut LiTaO<sub>3</sub>,” *Sensors and Actuators A: Physical* **193**, 87 (2013).
- <sup>59</sup>Y. Q. Fu, J. K. Luo, N. T. Nguyen, A. J. Walton, A. J. Flewitt, X. T. Zu, Y. Li, G. McHale, A. Matthews, E. Iborra, H. Du, and W. I. Milne, “Advances in piezoelectric thin films for acoustic biosensors, acoustofluidics and lab-on-chip applications,” *Progress in Materials Science* **89**, 31 (2017).
- <sup>60</sup>S. Fu, W. Wang, Q. Li, Z. Lu, Z. Chen, J. Luo, J. Shen, R. Wang, C. Song, F. Zeng, and F. Pan, “High-frequency V-doped ZnO/SiC surface acoustic wave devices with enhanced electromechanical coupling coefficient,” *Applied Physics Letters* **114**, 113504 (2019).
- <sup>61</sup>C. Deger, E. Born, H. Angerer, O. Ambacher, M. Stutzmann, J. Hornsteiner, E. Riha, and G. Fischerauer, “Sound velocity of Al<sub>x</sub>Ga<sub>1-x</sub>N thin films obtained by surface acoustic-wave measurements,” *Applied Physics Letters* **72**, 2400 (1998).
- <sup>62</sup>H. Nakahata, S. Fujii, K. Higaki, A. Hachigo, H. Kitabayashi, S. Shikata, and N. Fujimori, “Diamond-based surface acoustic wave devices,” *Semiconductor Science and Technology* **18**, S96 (2003).
- <sup>63</sup>R. O. Pohl, X. Liu, and E. Thompson, “Low-temperature thermal conductivity and acoustic attenuation in amorphous solids,” *Reviews of Modern Physics* **74**, 991 (2002).
- <sup>64</sup>T. Azuhata, M. Takesada, T. Yagi, A. Shikanai, S. Chichibu, K. Torii, A. Nakamura, T. Sota, G. Cantwell, D. B. Eason, and C. W. Litton, “Brillouin scattering study of ZnO,” *Journal of Applied Physics* **94**, 968 (2003).
- <sup>65</sup>A. W. Warner, M. Onoe, and G. A. Coquin, “Determination of Elastic and Piezoelectric Constants for Crystals in Class (3m),” *The Journal of the Acoustical Society of America* **42**, 1223 (1967).
- <sup>66</sup>D. Strauch, “Gan: Poisson ratio, young’s modulus, bulk modulus,” in *New Data and Updates for IV-IV, III-V, II-VI and I-VII Compounds, their Mixed Crystals and Diluted Magnetic Semiconductors*, edited by U. Rössler (Springer Berlin Heidelberg, Berlin, Heidelberg, 2011) pp. 409–412.
- <sup>67</sup>C. M. Flannery, M. D. Whitfield, and R. B. Jackman, “Acoustic wave properties of CVD diamond,” *Semiconductor Science and Technology* **18**, S86 (2003).
- <sup>68</sup>B. A. Auld, *Acoustic fields and waves in solids*, Vol. 2 (Krieger, 1990).
- <sup>69</sup>M. A. Hopcroft, W. D. Nix, and T. W. Kenny, “What is the Young’s Modulus of Silicon?” *Journal of Microelectromechanical*

- Systems* **19**, 229 (2010).
- <sup>70</sup>A. J. Hughes, “Elastic Surface Wave Guidance by  $(\Delta v/v)$  Effect Guidance Structures,” *J. Appl. Phys.* **43**, 2569 (1972).
- <sup>71</sup>Z. Shen, X. Han, C.-L. Zou, and H. X. Tang, “Phase sensitive imaging of 10 ghz vibrations in an aln microdisk resonator,” *Review of Scientific Instruments* **88**, 123709 (2017).
- <sup>72</sup>H. Tiersten, “Elastic surface waves guided by thin films,” *Journal of Applied Physics* **40**, 770 (1969).
- <sup>73</sup>R. Li, A. Oliner, and H. Bertoni, “Microwave network analyses of surface acoustic waveguides. i-flat overlay guides,” *IEEE Transactions on Sonics Ultrasonics* **24**, 66 (1977).
- <sup>74</sup>S. Markman, R. C. Li, A. Oliner, and H. Bertoni, “Microwave network analyses of surface acoustic waveguides. ii-rectangular ridge guides,” *IEEE Transactions on Sonics Ultrasonics* **24**, 79 (1977).
- <sup>75</sup>A. Love, “Some problems of geodynamics,” *Some Problems of Geodynamics* Publisher: Cambridge University Press, Cambridge (1911).
- <sup>76</sup>V. Bougrov, M. Levinshtein, S. Rumyantsev, and A. Zubrilov, *Properties of Advanced Semiconductor Materials GaN, AlN, InN, BN, SiC, SiGe* (John Wiley & Sons, Inc., New York, 2001) pp. 1–30.
- <sup>77</sup>“MolTech GmbH website sapphire al2o3,” [http://www.mt-berlin.com/frames\\_cryst/descriptions/sapphire.htm](http://www.mt-berlin.com/frames_cryst/descriptions/sapphire.htm), accessed: 2016-07-17.
- <sup>78</sup>L. Rayleigh, “On waves propagated along the plane surface of an elastic solid,” *Proceedings of the London Mathematical Society* **1**, 4 (1885).
- <sup>79</sup>M. T. Hill, Y.-S. Oei, B. Smalbrugge, Y. Zhu, T. De Vries, P. J. Van Veldhoven, F. W. Van Otten, T. J. Eijkemans, J. P. Turkiewicz, H. De Waardt, *et al.*, “Lasing in metallic-coated nanocavities,” *Nature Photonics* **1**, 589 (2007).
- <sup>80</sup>R. Oulton, G. Bartal, D. Pile, and X. Zhang, “Confinement and propagation characteristics of subwavelength plasmonic modes,” *New Journal of Physics* **10**, 105018 (2008).
- <sup>81</sup>P. E. Lagasse, I. M. Mason, and E. A. Ash, “Acoustic surface waveguides—analysis and assessment,” *IEEE Transactions on Microwave Theory and Techniques* **21**, 225 (1973).
- <sup>82</sup>J. N. Reddy, *Theory and analysis of elastic plates and shells* (CRC press, 2006).
- <sup>83</sup>B. Sinha and H. Tiersten, “Elastic and piezoelectric surface waves guided by thin films,” *Journal of Applied Physics* **44**, 4831 (1973).
- <sup>84</sup>P. E. Lagasse, I. M. Mason, and E. A. Ash, “Acoustic surface waveguides—analysis and assessment,” *IEEE Transactions on Microwave Theory and Techniques* **21**, 225 (1973).
- <sup>85</sup>L. Rayleigh, “Cxxii. the problem of the whispering gallery,” *The London, Edinburgh, and Dublin Philosophical Magazine and Journal of Science* **20**, 1001 (1910).
- <sup>86</sup>L. Rayleigh, “Ix. further applications of bessel’s functions of high order to the whispering gallery and allied problems,” *The London, Edinburgh, and Dublin Philosophical Magazine and Journal of Science* **27**, 100 (1914).
- <sup>87</sup>A. N. Oraevsky, “Whispering-gallery waves,” *Quantum Electronics* **32**, 377 (2002).
- <sup>88</sup>A. B. Matsko and V. S. Ilchenko, “Optical resonators with whispering gallery modes i: basics,” *IEEE J. Sel. Top. Quantum Electron* **12**, 3 (2006).
- <sup>89</sup>V. S. Ilchenko and A. B. Matsko, “Optical resonators with whispering-gallery modes-part ii: applications,” *IEEE Journal of selected topics in quantum electronics* **12**, 15 (2006).
- <sup>90</sup>M. R. Foreman, J. D. Swaim, and F. Vollmer, “Whispering gallery mode sensors,” *Advances in optics and photonics* **7**, 168 (2015).
- <sup>91</sup>T. J. A. Kippenberg, *Nonlinear optics in ultra-high-Q whispering-gallery optical microcavities*, Ph.D. thesis, California Institute of Technology (2004).
- <sup>92</sup>C. W. Hsu, B. Zhen, A. D. Stone, J. D. Joannopoulos, and M. Soljačić, “Bound states in the continuum,” *Nature Reviews Materials* **1**, 1 (2016).
- <sup>93</sup>Y. Chen, Z. Shen, X. Xiong, C.-H. Dong, C.-L. Zou, and G.-C. Guo, “Mechanical bound state in the continuum for optomechanical microresonators,” *New Journal of Physics* **18**, 063031 (2016).
- <sup>94</sup>A. Yariv, “Coupled-mode theory for guided-wave optics,” *IEEE Journal of Quantum Electronics* **9**, 919 (1973).
- <sup>95</sup>A. Hardy and W. Streifer, “Coupled mode theory of parallel waveguides,” *Journal of lightwave technology* **3**, 1135 (1985).
- <sup>96</sup>H. Haus, W. Huang, S. Kawakami, and N. Whitaker, “Coupled-mode theory of optical waveguides,” *Journal of Lightwave Technology* **5**, 16 (1987).
- <sup>97</sup>Z. Shen, W. Fu, R. Cheng, H. Townley, C.-L. Zou, and H. X. Tang, “Polarization mode hybridization and conversion in phononic wire waveguides,” *Applied Physics Letters* **115**, 201901 (2019).
- <sup>98</sup>Y. D. Dahmani, C. J. Sarabalis, W. Jiang, F. M. Mayor, and A. H. Safavi-Naeini, “Piezoelectric transduction of a wavelength-scale mechanical waveguide,” *Physical Review Applied* **13**, 024069 (2020).
- <sup>99</sup>A. Arnau, T. Sogorb, and Y. Jiménez, “A continuous motional series resonant frequency monitoring circuit and a new method of determining butterworth–van dyke parameters of a quartz crystal microbalance in fluid media,” *Review of scientific instruments* **71**, 2563 (2000).
- <sup>100</sup>M. Imboden and P. Mohanty, “Dissipation in nanoelectromechanical systems,” *Physics Reports Dissipation in nanoelectromechanical systems*, **534**, 89 (2014).
- <sup>101</sup>A. H. Safavi-Naeini, D. V. Thourhout, R. Baets, and R. V. Laer, “Controlling phonons and photons at the wavelength scale: integrated photonics meets integrated photonics,” *Optica* **6**, 213 (2019).
- <sup>102</sup>F. P. Payne and J. P. R. Lacey, “A theoretical analysis of scattering loss from planar optical waveguides,” *Optical and Quantum Electronics* **26**, 977 (1994).
- <sup>103</sup>S. Hughes, L. Ramunno, J. F. Young, and J. E. Sipe, “Extrinsic Optical Scattering Loss in Photonic Crystal Waveguides: Role of Fabrication Disorder and Photon Group Velocity,” *Physical Review Letters* **94**, 033903 (2005).
- <sup>104</sup>D. Melati, A. Melloni, and F. Morichetti, “Real photonic waveguides: guiding light through imperfections,” *Advances in Optics and Photonics* **6**, 156 (2014).
- <sup>105</sup>Q. Liu, H. Li, and M. Li, “Electromechanical Brillouin scattering in integrated optomechanical waveguides,” *Optica* **6**, 778 (2019).
- <sup>106</sup>K. Yasumura, T. Stowe, E. Chow, T. Pfafman, T. Kenny, B. Stipe, and D. Rugar, “Quality factors in micron- and submicron-thick cantilevers,” *Journal of Microelectromechanical Systems* **9**, 117 (2000).
- <sup>107</sup>R. H. Olsson III and I. El-Kady, “Microfabricated phononic crystal devices and applications,” *Meas. Sci. Technol.* **20**, 012002 (2009).
- <sup>108</sup>M. Maldovan, “Sound and heat revolutions in phononics,” *Nature* **503**, 209 (2013).
- <sup>109</sup>D. Hatanaka, I. Mahboob, K. Onomitsu, and H. Yamaguchi, “Phonon waveguides for electromechanical circuits,” *Nat. Nanotechnol.* **9**, 520 (2014).
- <sup>110</sup>C.-L. Zou, W. Fu, and H. X. Tang, “Surface acoustic gyroscope,” In Preparation (2016).
- <sup>111</sup>W. Fu, F.-J. Shu, Y.-L. Zhang, C.-H. Dong, C.-L. Zou, and G.-C. Guo, “Integrated optical circulator by stimulated Brillouin scattering induced non-reciprocal phase shift,” *Opt. Express* **23**, 025118 (2015).